



Flame stability optimization of cavity primary air-jet form in an augmentor

Yakun Huang^{a, b}, Xiaomin He^{a, *}, Huangwei Zhang^{b, **}, Zhixin Zhu^c, Huanyu Zhu^a

^a Jiangsu Province Key Laboratory of Aerospace Power System, College of Energy and Power Engineering, Nanjing University of Aeronautics and Astronautics, Nanjing, 210016, China

^b Department of Mechanical Engineering, National University of Singapore, Singapore, 117576, Singapore

^c School of Aeronautics and Astronautics, Zhejiang University, Hangzhou, 310027, China

ARTICLE INFO

Article history:

Received 20 May 2020

Received in revised form

19 July 2021

Accepted 12 August 2021

Available online 1 September 2021

Keywords:

Cavity

Air-jet form

Lean ignition

Lean blowout

Augmentor

TBCC

ABSTRACT

A trapped vortex cavity with a radial V-gutter flameholder is adopted to expand the flame stability of an augmentor. The improvement of flame stabilization limits is achieved experimentally by replacing the traditional slotted air-jet with the discrete-hole air-jet. The atomization characteristics of the air-assisted multi-point injector and the numerical fluid-structure are conducted to explain the results. Results indicate that a remarkable enhancement of the flame stability with discrete-hole air-jet is obtained in all conditions, while the slotted air-jet for the cavity leads to a failed ignition at 343 K except for the Mach number of 0.3. As the same passing area of the air-jet, the larger the aperture of the discrete hole, the better the flame stabilization performance. An increasing trend of lean blowout equivalence ratio is contributed by the increased Mach number. Whereas, the Mach number growth will lead to a reduction of lean ignition equivalence ratio at 343 K and 473 K, and a downward parabola is observed at 573 K. Eventually, the optimal flame stability performance is achieved in by the larger discrete space distance, which promotes the fuel/air mixture with the help of the recirculation zones between discrete holes.

© 2021 Elsevier Ltd. All rights reserved.

1. Introduction

Turbine-based combined cycle (TBCC) is undoubtedly regarded as one of the most promising hypersonic propulsion power systems, which effectively increases national defense and military deterrence [1]. The efficient and reliable ignition and reignition are indispensable for the combined combustor at high speed and low temperature [2]. The inlet conditions of the combustion may deteriorate sharply with the pressing applications of the combustor in high-altitude flights [3], so it is urgent to broaden the flame stabilization limits of the combustor. Previous investigations indicate that the cavity-based combustor can weaken the inlet disturbance and expand the operating range effectively [4].

A cavity-based combustor contains a cavity and several struts, in which two opposed air-jets with different heights form a stationary vortex over a wide range of mainstream conditions [5] that can hold

a stable flame with the injected fuel [6]. In general, an improvement of at least 40% in the operating range can be available when using the cavity-based combustor, as compared with the traditional gas turbine combustor [7]. Meanwhile, the ultra-compact and high-efficiency augmentor shows good application prospects [8], and the cavity-based augmentor has been demonstrated the characteristics of low resistance and a high thrust/weight ratio [9]. Hence, the promising cavity-based combustor deserves to be studied in depth and detail, significantly extending the flame stability limit [10].

As an advanced concept of the flameholder, the flow field [11] and combustion characteristics [12] of the cavity based on the slotted air-jets have been widely studied under the various inlet Mach number and temperature conditions [13]. It has already confirmed the benefits of a cavity-based combustor in aero-engines [14], ramjets [10], and scramjets [15]. To evaluate the application of the trapped vortex cavity (TVC), an encouraging result from the National Energy Technology Laboratory revealed that only ~17% of fuel-bound nitrogen was converted to NO_x [16]. Besides, Meyer [5] proved in his experiment that the lean blowout (LBO) limits were 50% below those for conventional combustors, and the reflight height could be reached at 12 km, which was 33.3% higher than that

* Corresponding author.

** Corresponding author.

E-mail addresses: hxm@nuaa.edu.cn (X. He), huangwei.zhang@nus.edu.sg (H. Zhang).

Nomenclature			
AMI	air-assisted multi-point injector	ϕ	equivalence ratio
E, R	combustor reference parameter	η	combustion efficiency, %
C_c, C_{pz}	volumes of the combustor	β	vortex angle of the critical point and fore-wall
H	height, mm	σ	surface tension, N/m
H_r	lower calorific value	ρ	density, kg/m ³
L	length, mm	x, y, z	axial, radial and spanwise coordinates, respectively
LPSA	Malvern laser particle size analyzer	$Z1, Z2, Z3$	sections
Ma	Mach number	<i>Subscript</i>	
m	mass flow rate, kg/s	1	core stream inlet
PDPA	phase doppler particle analyzer	2	bypass stream inlet
P	pressure, Pa	3	combustion section
ΔP	pressure drop, Pa	a	inlet of the after-wall
q	fuel/air ratio	ac	cavity
SMD	Sauter mean diameter, μm	f	inlet of the fore-wall
T	temperature, K	fuel	RP-3 kerosene liquid fuel
TBCC	turbine based combined cycle	lg	ignition
TVC	trapped vortex cavity	LBO	lean blowout
V	velocity	main	mainstream
λ_r	effective evaporation	sf	flame propagation
v	velocity, m/s	B	point B

in conventional combustors. Then, numerous efforts were conducted to expand the flame stability of the cavity-based combustor by improving the 'trapped' vortex structure and fuel/air mixing, such as adjusting cavity size [17], innovating the fuel supply mode [18], and optimizing the jet flow [19,20].

Initially, the rules for sizing cavities were investigated to keep a stable flame with a minimum drag [21]. The cavity surrounding the casing with several struts radially hanging on the fore-wall can reduce the equivalence ratio (ϕ) of LBO and improve the combustion efficiency (η) [22]. These results indicated that a stable vortex or dual-vortex in the cavity stabilized the flame well, but the injection problem was not solved. After that, the injector's optimum location was found to be above the centerline of the fore-wall in the cavity, and the lowest LBO limits were achieved by dual-vortex fluid structure [16]. A rapid fuel/air mixing performed in the cavity leads to higher combustion efficiency and lower NO_x emission [23]. The extraordinary distribution and mixing of the fuel and air were facilitated by 54 injectors, which efficiently improved flame stability and combustion efficiency [5]. As mentioned above, the dual-vortex in the cavity is directly affected by the momentum of the flux ratio. Besides, Hsu et al. [24] found that the streamwise vortex established in the cavity could be strengthened by injecting a high momentum air-jet (or secondary air-jet) from the after-wall. Also, the effect on the angle and height of the fore and after air-jets of the cavity had been experimentally studied to improve the stability of the vortex in the cavity [25].

In conclusion, there are many ways to strengthen the flame stability of the cavity, among which the structural adjustment [26,27] and fuel supply mode [12,21] are researched more extensively, while the method of primary air-jet in the cavity is lacking exploration. The flame stability has been significantly improved with a rapid fuel/air mixing, achieved by injection hole [28]. Besides, the turbulence caused by air passing through the holes promotes the mixing of fuel and air [29], and fuel droplets move around the primary vortex in the cavity provides a longer residence time for the fuel/air mixing. Unfortunately, few attempts have been made so far to unravel the effect of air-jet injected from slotted or punched coupling with the fuel supply device of the evaporation tube on the cavity flame stability, which may be beneficial for

homogeneity of fuel/air mixture. Therefore, in order to fill in the gaps of flame stabilization in different air-jet of the cavity, the effect of primary air-jet form on lean ignition and lean blowout limits need to be fully understood.

In this paper, a rectangular combustor with a cavity and a radial V-gutter flameholder is designed as a part of the TBCC augmentor. Three kinds of discrete-hole air-jet and one slotted air-jet were adopted to experimentally investigate the effect of primary air-jet form in the cavity on combustion characteristics. The test rig is carefully designed and fabricated based on our previous work [30]. This paper focuses on improving the ignition and lean blowout through the slight change of the primary inlet in the cavity. This paper's remainder first introduces the experimental model, setups, and primary air-jet forms in section 2. Detailed performance of ignition, lean blowout, and discussion are then presented in section 3. The last section comes to the main conclusions.

2. Combustor and experimental/numerical setups

2.1. Combustor design

Fig. 1 shows 2-D schematics and the photograph of the augmentor with a cavity and a radial V-gutter flameholder, which draws the center section of a rectangle combustor with a size of 120 mm × 144 mm × 1360 mm. As shown, the augmentor consists of a diffuser, a cavity, an air-assisted multi-point injector (AMI), a V-gutter flameholder, a spark plug, and two inlets, which are core stream inlet₁ and bypass stream inlet₂, respectively. In this paper, the TBCC is operating at ramjet operating mode. The ratio of the diffuser is 1.38. The basal design of the cavity with a slotted inlet has already been conducted by previous numerical simulations and combustion tests [31]. Meanwhile, the air-assisted multi-point injector (AMI) has also been investigated to match well with the cavity combustion in the main chamber [32]. It makes sense to combine the advantages of AMI with the cavity-based augmentor and optimize it. The RP-3 liquid fuel is injected vertically onto the splash plate by a plain orifice with a diameter of 0.5 mm. The diameter of the multi-hole tube is 10 mm, in which the evaporating tube has 20 holes of diameter 2 mm with a pitch of 5.7 mm.

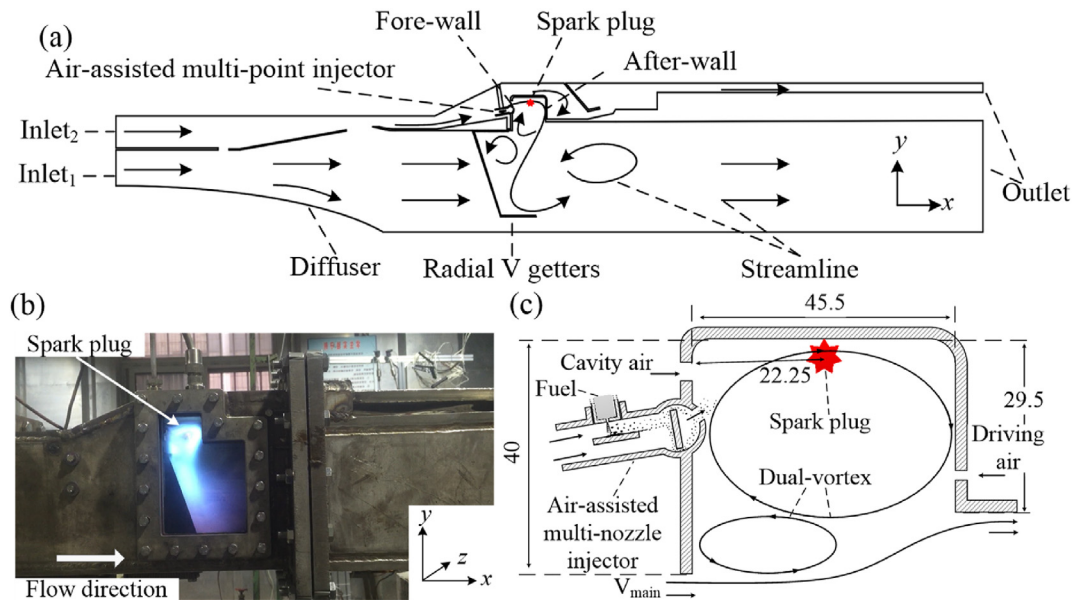


Fig. 1. 2-D schematic and a photograph of augmentor at the center section: (a) schematic of the augmentor, (b) a photograph of augmentor, (c) schematic of the injector. All dimensions in mm.

The 2-D schematic of the cavity and AMI in section 20 mm from the center is depicted in Fig. 1(c). The length of the cavity is 45.5 mm, and the depths of the fore-wall and the after-wall are 40 mm and 29.5 mm, respectively. The secondary air-jet flows through a slot on the after-wall with a width of 1.6 mm. Besides, one slotted air-jet and three kinds of discrete-hole air-jet are built by a processed fore-wall plate with the slot or discrete holes, as shown in Fig. 2. Here, the slot inlet with a width of 1.6 mm and discrete holes with different diameters are set as 2.5 mm, 3.4 mm, and 5.0 mm with the same inlet passing area. The slot inlet is labeled as Case 1, and the discrete holes inlets are marked as Case 2, Case 3, and Case 4, respectively. Then, the flame spread out from the spark plug with 12 J (8 Hz) installed at the center of the bottom wall with a z-axis distance of 20 mm to the center section. Additionally, a successful ignition is marked by the observation, through an optical quartz glass, that the steady flame fills the entire cavity.

As mentioned above, the primary and secondary air jets inject into the cavity with a height difference that will form a dual-vortex structure. The cavity is filled with the primary vortex, and the secondary vortex appears in the corner of the fore-wall, meeting the mainstream. Therefore, the secondary vortex separates the primary vortex from the mainstream, protecting the stability of the primary vortex and exchanging energy and composition [33]. However, the dual-vortex structure is destroyed into an incomplete single vortex when the fluid in the cavity is attracted by the low-

pressure area behind the radial V-gutter flameholder at the central section, as shown in Fig. 1(a). A noteworthy feature of the fore-wall is that little air mixed with fuel will enter into the cavity from AMI. The fuel/air mixture flows into the primary vortex and completes the ignition to establish a stable flame zone, igniting the whole combustor.

2.2. Air-assisted multi-point injector

The 3-D structure of the air-assisted multi-point injector is shown schematically in Fig. 3. The air inlet size is set to 8 mm × 16 mm as a reference for the computation of mass flow rate. The diameter of the multi-holes tube is 10 mm, which distributes 20 holes of diameter 2 mm, and the pitch of holes is 5.7 mm. Two plates reached a thickness of 1 mm are installed at the center of the inlet and multi-holes tube. The diameter of the plain orifice is 0.5 mm, which is mounted inside the air-assisted multi-point injector. The RP-3 liquid fuel is injected vertically into the splash plate. Then, a part of fuel departs into droplets, and other parts form the fuel film. Thereby, the fuel film, moving and mixing with the airflow, gradually becomes thinner and breaks into droplets (as schematically shown in Fig. 1(c)). Finally, the fuel/air mixture enters the trapped vortex through multiple holes.

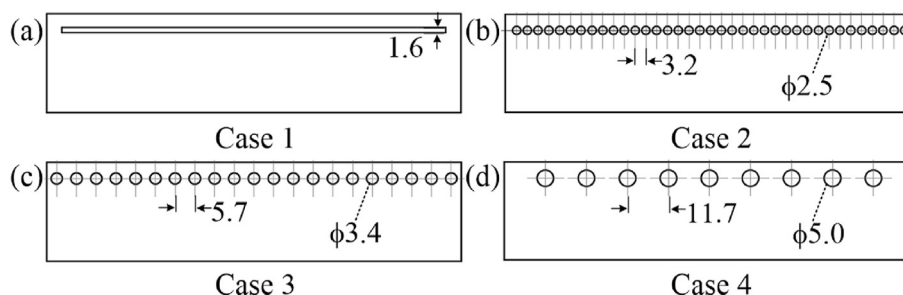


Fig. 2. The inlet structures in the fore-wall inlet structure of the cavity. All dimensions in mm.

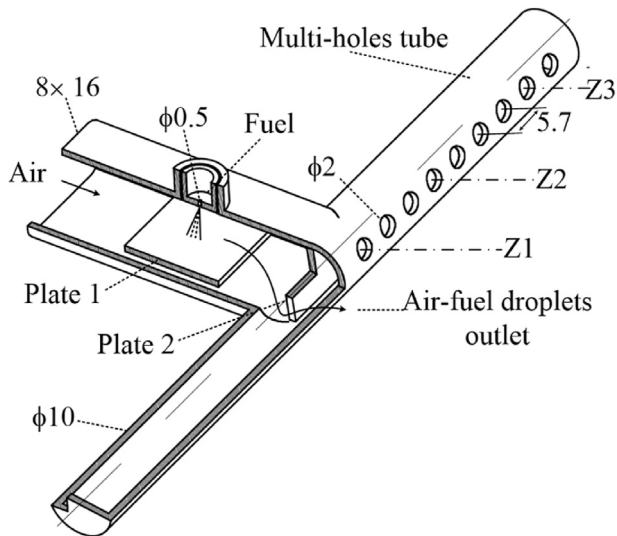


Fig. 3. 3-D structure of air-assisted multi-point injector. All dimensions in mm.

2.3. Experimental setup

2.3.1. Experimental system

Experimental studies are conducted in a sector channel with an air supply and exhaust system, which is schematically shown in Fig. 4. The experimental system is divided into four parts: air supply device, fuel supply system, pre-heater, and the test section. The air supply device can provide the dehumidified air with a maximum pressure of 0.8 MPa and a maximum mass flow total rate of 1.5 kg/s. The incoming air is divided into two paths, one of them is electrically heated, and the other is pre-heated by combustion with RP-3 liquid fuel. The electric heater can raise the airflow temperature by 200 K, while the pre-burner can heat the room temperature air to a maximum of 873 K. Here, the oxygen mass fraction is maintained at 23.20%–22.35%, as the combustion efficiency of the pre-burner approaches to 99.8%. Besides, an orifice flowmeter with an accuracy of 0.57% is used to measure the total mass flow rate. The pressure and temperature at the inlet are measured by the pressure gauge and the K-type thermocouple, which are both mounted 50 mm upstream of the test section. The uncertainties of the K-type thermocouple and pressure gauge are both 0.4%. Also, the unvitiated air from the electrical heater and the vitiated air from the pre-burner is supplied to the core inlet and the bypass inlet of the test rig, respectively. The fuel is pressurized by the pump so it can be injected into the experimental model, and the fuel mass flow rate is determined by the pressure gauge. Furthermore, the relationship between the fuel mass flow rate and pressure drop is

calibrated before the test. The uncertainties of the pressure gauges and the electronic scale are 0.4% and 0.01%, respectively. Then, the correlation is supplied as follows:

$$\Delta P_{fuel} = 0.1249m_{fuel}^{1.9665} \quad (1)$$

where the ΔP_{fuel} is the fuel pressure drop, the m_{fuel} is the mass flow rate of the fuel.

The combustor has two inlets: core inlet and bypass inlet, denoted by subscripts 1 and 2. In this paper, the influence of inlet structure on ignition and blowout performance is mainly studied. Therefore, the core inlet parameters are kept the same, while the parameters of the bypass inlet are changed within a specific range. The detailed operational parameters for the combustor are listed in Table 1.

The characteristics of fuel atomization and distribution in the trapped vortex substantially affect the performance of ignition and blowout limits. In order to understand the flame stability in-depth, the atomization characteristics of AMI were studied experimentally. Fig. 5 shows the experimental setup for the Malvern laser particle size analyzer (LPSA), measuring particle size from 4.6 to 323 μm with a maximum measurement uncertainty of 1.75%. LPSA can measure the particle size and distribution within a laser beam located 20 mm downstream of the AMI. The widely accepted R-R distribution [34] is used to analyze the particle size distribution by LPSA, and the results of AMI obtained by phase doppler particle analyzer (PDPA) also conform to R-R distribution [32]. The particle size and distribution on the three sections of Z1, Z2, and Z3 were measured, as shown in Fig. 3. The air of AMI is provided by the high-pressure cylinder, whose mass flow rate is obtained by the flowmeter with an uncertainty of 1.5%. At the same time, the filtered fuel is pumped into the AMI, and the fuel mass flow rate is calculated by pressure value before the plain orifice of AMI. Additionally, the test was conducted at room temperature and pressure with the inlet Mach number of AMI changing from 0.3 to 0.6. The equivalent ratios are 0.4, 0.6, 0.8, and 1.0, respectively, and the pressure drop can be calculated by Eq. (1).

2.3.2. Experimental uncertainty

Errors in the experimental value can be reduced by standardizing the experimenter and unifying the measurement. However, inherent uncertainty exists in the measurement devices or measurement environment, which can be weakened by repeated tests.

Table 1
Summary of experimental conditions.

Ma_1	T_1/K	Ma_2	T_2/K	P/MPa
0.18	473	0.30–0.70	343–573	0.101

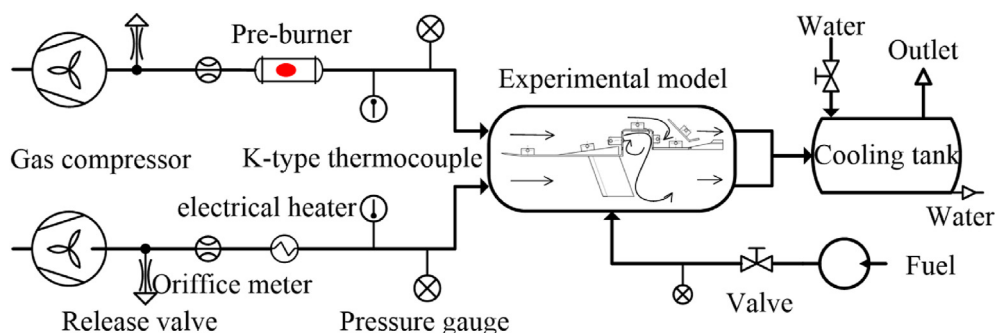


Fig. 4. Experimental setups for combustion.

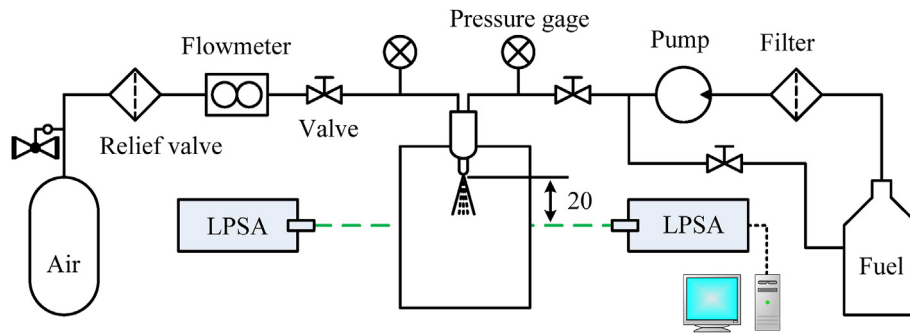


Fig. 5. Experimental setups for Malvern laser particle size analyzer (LPSA). All dimensions are in mm.

To evaluate the results' uncertainty more precisely, the T-distribution assumption is adopted indirect measurement with the confidence factor $z = 1.96$. Besides, the probability of confidence is 95%. One of the repeatability tests is conducted in a manner by fixing the airflow rate and temperature of two inlets at 0.457 kg/s, 0.137 kg/s, and 473 K, respectively, and running the combustor at an equivalence ratio of 0.2 for five times. The details of the uncertainty analysis are shown in Table 2.

2.4. Experimental procedure

In order to accurately evaluate the effect of primary air-jet form on the flame stability of the cavity, a series of flame stability limit tests were performed. The numerical non-reaction fluid structure is used to explain the change in flame stability. Also, the measured characteristics of fuel droplets injected from AMI help understand the lean ignition and blowout limits' development trend.

The detailed procedures of lean ignition and blowout limits are conducted to evaluate the effect of inlet primary air-jet form on the flame stability limits. Fig. 6 shows the experimental procedures of the lean ignition and blowout of spray kerosene liquid fuel. The lean ignition limit measurement procedure is shown in Fig. 6(a). Specifically, the spark plug begins to discharge continuously, and then the fuel is supplied with the pressure drop increasing gradually. Once the flame has been ignited successfully, the pressure drop ΔP_0 is marked as the initial pressure drop. After that, the lowest pressure drop of successful ignition can be obtained by continuously reducing the fuel pressure drop ΔP . Here, the $\Delta P = 0.005$ MPa. Similarly, the lean blowout procedure, shown in Fig. 6(b), is calculated by the lowest fuel pressure drop. Besides, the lowest pressure drop is determined by the minimum pressure drop ΔP_j , which cannot hold the flame. In this work, the ignition and extinction criteria are determined by the flame image [36]. When the observed flame image is generated and develops steadily, the ignition is considered successful; otherwise, the flame is extinguished.

Table 2
Physical quantities with their uncertainties.

Variable	Means	Uncertainties
Core stream inlet mass flow rate, kg/s	0.137	0.0008
Bypass stream inlet mass flow rate, kg/s	0.457	0.002
Inlet temperature, K	473	1.33
Core stream inlet Mach number	0.08	0.0004
Bypass stream inlet Mach number	0.3	0.0015
Equivalence ratio	0.2	0.0005
Fuel mass flow rate, 10^{-3} kg/s	1.84	0.0019

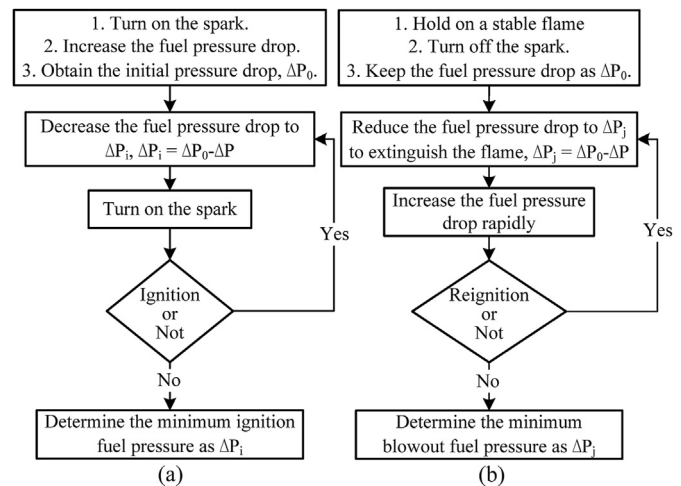


Fig. 6. Experimental procedures of (a) spark ignition and (b) lean blowout.

2.5. Numerical setups

Commercial CFD software is employed to perform computational fluid dynamics through the finite volume technique with a second-order upwind discretization. Two inlets are both specified as a mass flow inlet boundary and the outlet as a pressure boundary. The Mach number of inlet₁ and inlet₂ are kept as 0.08 and 0.2, respectively. Besides, two inlet temperature values are 473 K. Additionally, the outlet's pressure is set at 0 Pa with the operating pressure kept as 101,325 Pa. To match the experimental environment, the no-slip wall boundary is adopted on all wall surfaces. Moreover, an ideal gas is used for the present simulation.

2.5.1. Turbulence model

Two-equation models Shear stress transport (SST) $k-\omega$ and $k-\epsilon$ are widely adopted in the numerical calculation of the cavity flow field [37]. Comparing numerical results of different turbulence models and experimental data are performed to find the most appropriate numerical method by Jin [33]. The results suggest that the standard $k-\epsilon$ turbulence model can better predict the fluid structure of a cavity-based combustor. The model structure in this paper is similar to previous studies, the standard $k-\epsilon$ model is adopted [21]. Besides, the standard wall functions are adopted with the most y^+ values larger than 30 and less than 100. The transport equations of turbulence kinetic energy, k , and its rate of dissipation, ϵ , can be expressed as:

$$\frac{\partial}{\partial t}(\rho k) + \frac{\partial}{\partial x_i}(\rho k u_i) = \frac{\partial}{\partial x_j} \left[\left(\mu + \frac{\mu_t}{\sigma_k} \right) \frac{\partial}{\partial x_j} k \right] + P_k + G_b - \rho \epsilon - Y_M \tag{2}$$

$$\frac{\partial}{\partial t}(\rho \epsilon) + \frac{\partial}{\partial x_i}(\rho \epsilon u_i) = \frac{\partial}{\partial x_j} \left[\left(\mu + \frac{\mu_t}{\sigma_\epsilon} \right) \frac{\partial \epsilon}{\partial x_j} \right] + C_{1\epsilon} \frac{\epsilon}{k} (P_k + G_{3\epsilon} G_b) - C_{2\epsilon} \rho \frac{\epsilon^2}{k} \tag{3}$$

where, P_k is the generation of turbulence kinetic energy, G_b is the buoyancy generation of turbulence kinetic energy, Y_M is the contribution of the fluctuating dilatation incompressible turbulence to the overall dissipation rate, $-\rho \epsilon$ is the dissipation of the turbulence kinetic energy; meanwhile, the $C_{1\epsilon} \frac{\epsilon}{k} P_k, C_{1\epsilon} \frac{\epsilon}{k} G_{3\epsilon} G_b, C_{2\epsilon} \rho \frac{\epsilon^2}{k}$ represent the generation term, the effect of buoyancy term, and the dissipative term of the ϵ , respectively. The constants $C_{1\epsilon}, C_{2\epsilon}$, and $C_{3\epsilon}$ are 1.44, 1.92, and 0, respectively.

2.5.2. Mesh generation

The grid topologies for the three-dimensional combustor, taking the part of Case 1 for an example, are shown in Fig. 7. The flow field is artificially locally encrypted in the cavity to satisfy the detailed research. Therefore, fine meshes are used for fore-wall, after-wall inlets, and air-assisted multi-nozzle injector of the cavity as seen in the insert, which shows the cavity region marked by the white rectangle. Also, all the structural parameters are consistent with the experimental model.

2.5.3. Grid independent test and discretization error estimation

The fluid grids described previously are termed as standard version with 9,473,105 mesh cells. Two dense versions of grids with fine (11,747,907 mesh cells) and coarse (6,790,101 mesh cells) resolution are employed to calculate the steady flow field to study grid sensitivity. The radial profiles of the mean axial velocity at line 1 ($x = 0.653 \text{ m}$ and $z = 0$) in the x - y plane calculated by all versions are illustrated in Fig. 8. Two overlapping curves corresponding to the standard version and fine version indicate that accurate prediction can be achieved with both versions, except for several parts. Then, the standard version is chosen and predicted the total pressure recovery coefficient and temperature distribution to conduct the comparison between the numerical and experimental results, as shown in Fig. 9. The inlet parameters for comparison are detailed in Table 3. The numerical convergence criteria for continuity is 10^{-4} , while that for k and ϵ are 10^{-6} and 10^{-5} . The predicted temperature distribution reproduces the experimental results well under the condition of Case 1, in which the maximum error is 5.3%.

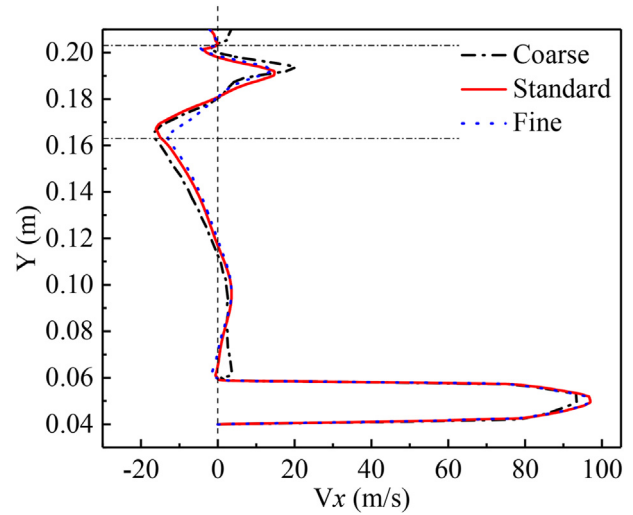


Fig. 8. Radial profiles of mean axial velocity at line 1.

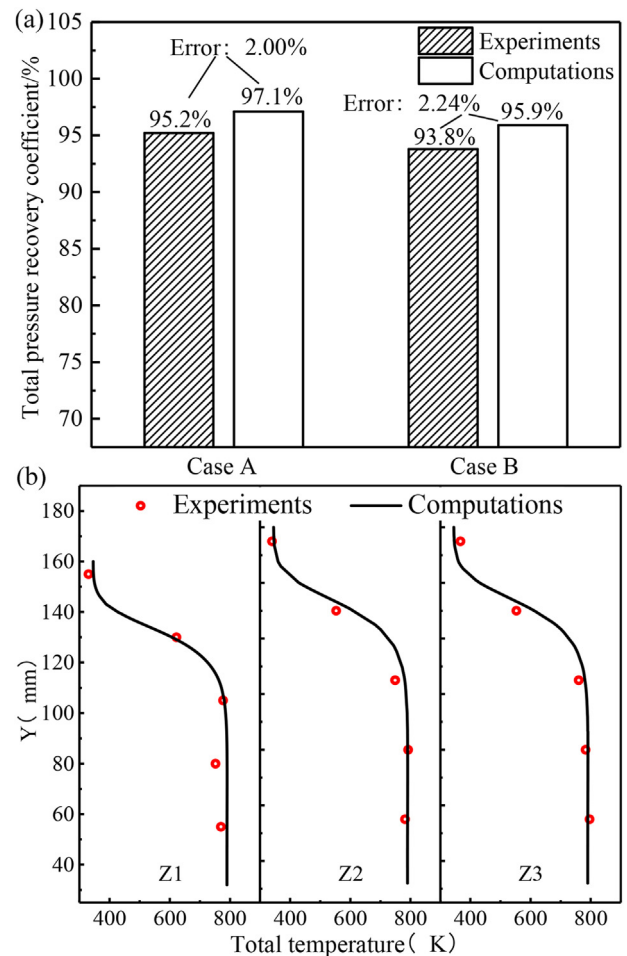


Fig. 9. Comparison between test and numerical simulation with (a) total pressure recovery coefficient in Case A and Case B, (b) outlet temperature distribution of Case A.

Besides, the total pressure recovery coefficient errors in Case A and Case B are 2% and 2.24%, respectively. Hence, the standard version's mesh with the standard k - ϵ model is relatively valid in this paper.

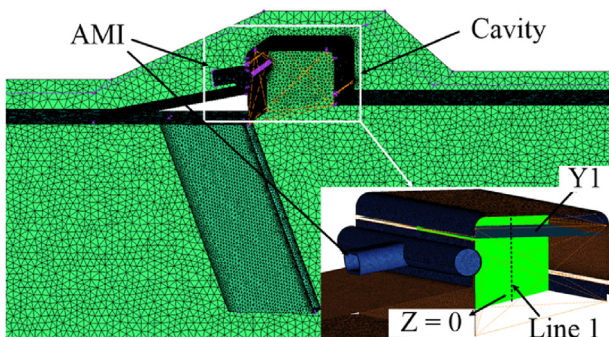


Fig. 7. Unstructured meshes for Case 1 of cavity piloted augmentor.

Table 3
Conditions of the numerical calculation.

Parameters	m_1 [kg/s]	T_1 [K]	P_1^* [MPa]	m_2 [kg/s]	T_2 [K]	P_2^* [MPa]
Case A	0.472	343	0.166	0.472	790	0.157
Case B	0.869	602	0.186	0.124	602	0.158

2.5.4. Flow distribution

The inlet structure of the cavity is designed with the same passing area, which demonstrates that the cumulative area of discrete holes in Case 2 to Case 4 is the same as that of the slot in Case 1. As mentioned in Fig. 2, the slotted-inlet is marked as Case 1, and the discrete-holes inlets are labeled as Case 2, Case 3, and Case 4. The flow distribution of Case 1 to Case 4 for a cavity is calculated to determine the proportion of the airflow rate of each part in the bypass inlet airflow rate. The total inlet airflow into the cavity is divided into primary airflow, secondary airflow, and AMI airflow, which are listed in Table 4. The average total airflow rate of the cavity is 3.66% of the bypass inlet airflow in all cases, and the flow distribution perfectly meets the design requirements.

3. Results and discussion

Repetitive experiments of ignition and lean blowout are carried out to obtain the average value of the equivalence ratio. Besides, the numerical fluid structure is calculated to help understand the flame stabilization in the cavity. Simultaneously, detailed results of drop-size distribution and volumetric cumulative distribution are used to understand the evolution of the flame stability limits.

3.1. Combustion tests results

Four types of the inlet structure on the fore-wall are designed to investigate the effect of the inlet structure on the lean ignition and blowout performance of a cavity piloted augmentor. The effect is directly explored by the combustion test in terms of ignition and lean blowout limit. Additionally, the equivalence ratio corresponding to the lowest fuel pressure drop, in which the fuel/air mixture can be ignited, is regarded as the lean ignition equivalence ratio [38]. Besides, the lean blowout equivalence ratio is corresponding to the lowest fuel/air ratio, at which point the flame disappears due to decreased fuel mass flow rate and cannot be reignited when increasing the fuel mass flow rate. The fuel/air ratio and the equivalence ratio are expressed as $q_{LBO} = m_{fuel}/m_{ac}$ and $\phi = q_{LBO}/q_{st}$. Here, the q_{LBO} is the fuel/air ratio, m_{fuel} is the fuel flow rate for AMI, m_{ac} is the total airflow rate in a cavity, ϕ is the equivalence ratio, and q_{st} is the stoichiometric fuel/air ratio, which is 0.0672 for the RP-3 liquid fuel.

3.1.1. Lean ignition limits

The lean ignition limits of the inlet structure parameters in the cavity piloted augmentor were evaluated using the equivalence ratios plotted in Fig. 10. The tendencies of the lean ignition equivalence ratio at $T_2 = 343$ K and 473 K decrease with the Mach number increasing. In comparison, the ignition equivalence ratio at

Table 4
The flow distribution for the cavity by numerical computation.

Parameters	Cavity air/%	Driving air/%	AMI air/%	Total/%
Case 1	1.66	1.47	0.56	3.69
Case 2	1.57	1.54	0.56	3.67
Case 3	1.55	1.52	0.56	3.63
Case 4	1.61	1.49	0.56	3.66

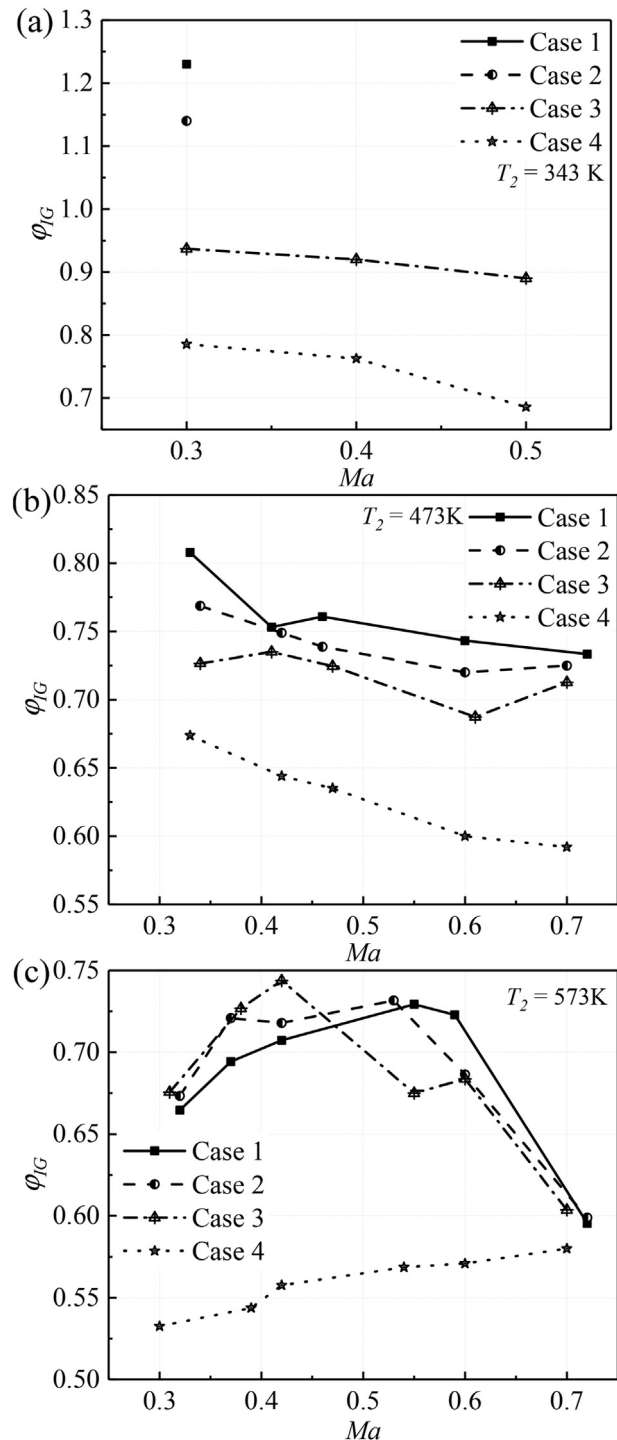


Fig. 10. Ignition equivalence ratio of combustor with various Mach numbers at: (a) $T_2 = 343$ K, (b) $T_2 = 473$ K, (c) $T_2 = 573$ K.

$T_2 = 573$ K has a parabola tend under the condition of Case 1 to Case 3. A successful ignition can only be achieved with the Mach number less than 0.3 at the temperature of 343 K in Case 1 and Case 2. Overall, a decreasing trend of the lean ignition equivalence ratio has been contributed by the change of inlet structure from slot to discrete holes. The worst performance of lean ignition occurs at $T_2 = 343$ K and $Ma_2 = 0.3$, corresponding to Case 1, whose ϕ_{IG} is 1.23 and 7.32%, 23.82%, and 36.14% larger than that in Case 2 to Case 4, respectively. Besides, the increased inlet Mach number leads a

diminution in equivalence ratio of lean ignition, in which the $\phi_{IG} = 0.686$ in Case 4 at $T_2 = 343$ K and $Ma_2 = 0.5$ is 12.72% and it is smaller than that at $T_2 = 343$ K and $Ma_2 = 0.3$. Four similar curves appear at $T_2 = 473$ K, which is strong evidence that the equivalence ratio of lean ignition becomes smaller with a growth of the Mach number. Furthermore, the averaged lean ignition equivalence ratio in Case 4 is 0.629, which is 20.79%, 20.14%, and 14.03% smaller than that in Case 1 to Case 3, respectively. However, a different tendency of the lean ignition equivalence ratio appears at $T_2 = 573$ K, where the equivalence ratios of Case 1 to Case 3 decrease after increasing. Compared to Case 1, the worse performance points of the lean ignition of Case 2 and Case 3 are obtained when the Mach number is less than 0.50, while the better one happens when the Mach number is larger than 0.55. It is worth noting that the lowest lean ignition equivalence ratio with an increasing trend occurs in Case 4, which means that the inlet structure of discrete holes can effectively improve the ignition performance. The larger the hole is, the better the optimization will be. Additionally, the approximate ignition equivalence ratio at $Ma_2 = 0.7$ in Cases 1 to 3 is about 0.599, which is 3.28% larger than that in Case 4.

3.1.2. Lean blowout limit

Fig. 11 shows the lean blowout equivalence ratio with the variation of inlet Mach number, temperature, and inlet structure of the cavity. As expected, the maximum LBO equivalence ratio is contributed by Case 1, while the minimum LBO equivalence ratio is acquired by Case 4. This phenomenon indicates that the discrete holes inlet is more beneficial to reduce the LBO equivalence ratio than the inlet structure of the slot. The increase in Mach number increases the LBO equivalence ratio, whereas the growth of the inlet temperature will lead to a drop in the LBO equivalence ratio. Fig. 11(a) shows that the LBO equivalence ratio corresponding to Case 3 and Case 4 has a linear growth with the increase of the inlet Mach number. As mentioned above, only at $Ma_2 = 0.3$ can the flame keep be stabilized in the cavity of Case 1 and Case 2. Also, the biggest LBO equivalence ratio of Case 1 is 0.860, which is 2.87%, 32.31%, and 45.76% larger than that in Cases 2 to 4, respectively. At the same time, the LBO equivalence ratios of Case 3 and Case 4 increase 46.07% and 50.07% with the Mach number varies from 0.3 to 0.5. Three LBO equivalence ratio curves with the same trend and approximate value appear in Case 1 to Case 3, which is mainly caused by the evaporation of the fuel droplets, as shown in Fig. 11(b) and (c). When the temperature is more significant than 473 K, the fuel droplets start to evaporate, which weakens the mixing effect of the primary air-jet form. However, the LBO equivalence ratio in Case 3 still has a slight advantage, which averagely reduces 4.60% and 6.31% than that in Case 1 at $T_2 = 473$ K and $T_2 = 573$ K, respectively. Besides, the lean blowout performance of Case 4 has been significantly improved compared with Case 1. The lowest LBO equivalence ratio is measured at $T_2 = 573$ K and $Ma_2 = 0.3$, which is 0.240 and 68.25% smaller than that in Case 1. All the above descriptions have proved the optimization effect of the discrete-hole inlet on the lean blowout performance.

Generally, increased Mach number would lead to two opposite effects. First, the acceleration of the air stream shortens the mixture residence time, which may reduce flame stability. Secondly, it may also increase the aerodynamic force and hence enhance the broken effect of fuel droplets. Here, a novel fuel supply device, an air-assisted multi-point injector, was designed for the cavity. The fuel droplet size is highly correlated with the inlet temperature and Mach number. Therefore, the lean ignition and blowout equivalence ratios show different trends with the increase of the inlet Mach number at the different inlet temperatures. At the low temperatures of 343 K and 473 K, the poor fuel evaporation happens during the ignition process, and the ignition equivalence ratio

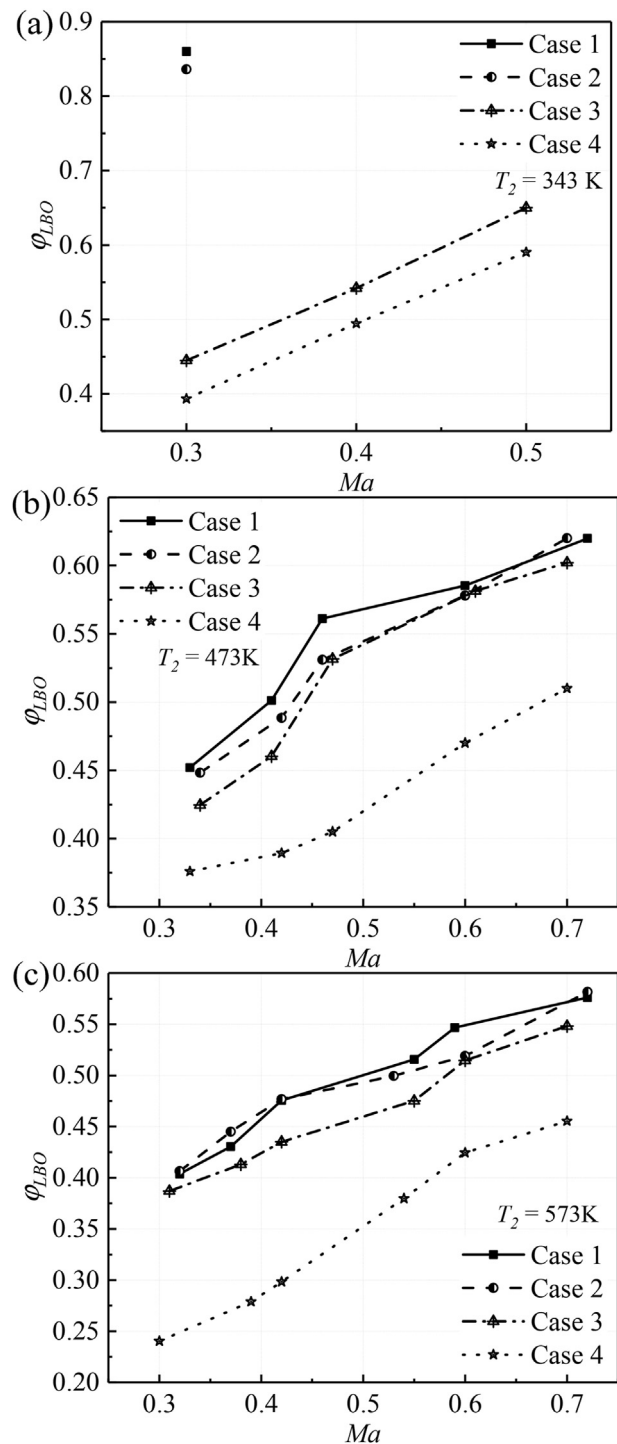


Fig. 11. Lean blowout equivalence ratio of combustor with various Mach numbers at: (a) $T_2 = 343$ K, (b) $T_2 = 473$ K, (c) $T_2 = 573$ K.

gradually decreases with the increase of Mach number, as shown in Fig. 10(a) and (b). When the inlet temperature maintains 573 K, effective fuel evaporation can be achieved in the ignition process. As shown in Fig. 10 (c), the increased Mach number in the lower range leads to an increasing trend of the lean ignition equivalence ratio; whereas, a continued increase in the higher range will cause the decreasing trend. In the lean blowout process, the fuel droplet evaporated efficiently by the pre-heated evaporation tube, indicating that the lean blowout performance worsens with the inlet

Mach number growth, as shown in Fig. 11. The specific analysis can be seen in section 3.2.

3.2. Numerical results and analysis

The ignition and lean blowout are complex processes, the coupling of energy, atomizer characteristic, and flow field, analyzed by the non-reaction flow field [33] or spray characteristic [39]. Previous studies have proved the time-scale theory can explain the flame stability of the cavity with dual-vortex well. The reason for ignition and lean blowout changes can be legitimately analyzed by the numerical flow field [40]. Here, the numerical calculation with the theoretical analysis can help to understand the results better.

The velocity vectors in the cavity of Case 1 are plotted in Fig. 12. Fig. 12(a) shows that the fluid injected from the AMI and primary inlet in the cavity flows to the negative direction of the y-axis. However, the classical dual-vortex structure inside the cavity appears in the section of $z = 20$ mm, as shown in Fig. 12(b), which is identical to the study of Jin [41] and Li [40]. Obviously, the primary vortex with the clockwise curl occupies the most space of the cavity. The secondary vortex appears between the primary vortex and mainstream, a tiny corner vortex with a counterclockwise rotation.

Fig. 13 demonstrates the schematic of flame stability in the

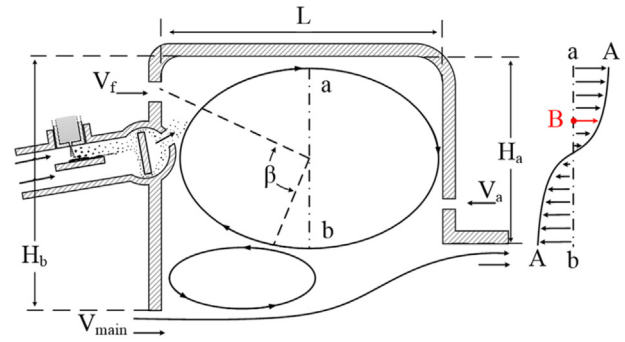


Fig. 13. Schematic of flame stability in a trapped vortex cavity.

trapped vortex cavity in the $z = 20$ mm section. It can be considered that the fuel/air mixture is thoroughly mixed when it enters the trapped vortex zone with the help of an AMI fuel supply device. A section a-b with the profile of velocity A-A is randomly selected in the trapped vortex. There must exist a point B that can stabilize the flame, where the airflow velocity is the same as the flame propagation velocity and the direction is opposite, denoted as

$$V_{sf} = V_B \quad (4)$$

where V_{sf} is the flame propagation velocity, V_B is the airflow velocity of point B.

It is worth noting that point B will move downstream along the streamline of the trapped vortex to the critical point of flame stability as the inlet velocity, V_f , gradually increases. The critical point, namely the separation point of the primary and secondary vortices, is located at the boundary of the primary vortex and forms an angle of β between the vortex core and the inlet of the fore-wall. Then, the lean blowout will occur if the V_f continues to increase. Hence, if the droplets are thin enough and evenly distributed, the growth of Mach number can lead to an offensive performance of lean ignition and lean blowout, which means that the increase of Mach number will contribute to the enlarged lean ignition and lean blowout equivalence ratios.

For completeness, four approximately overlapping radial profiles of the axial velocity at $x = 653$ mm in the section of

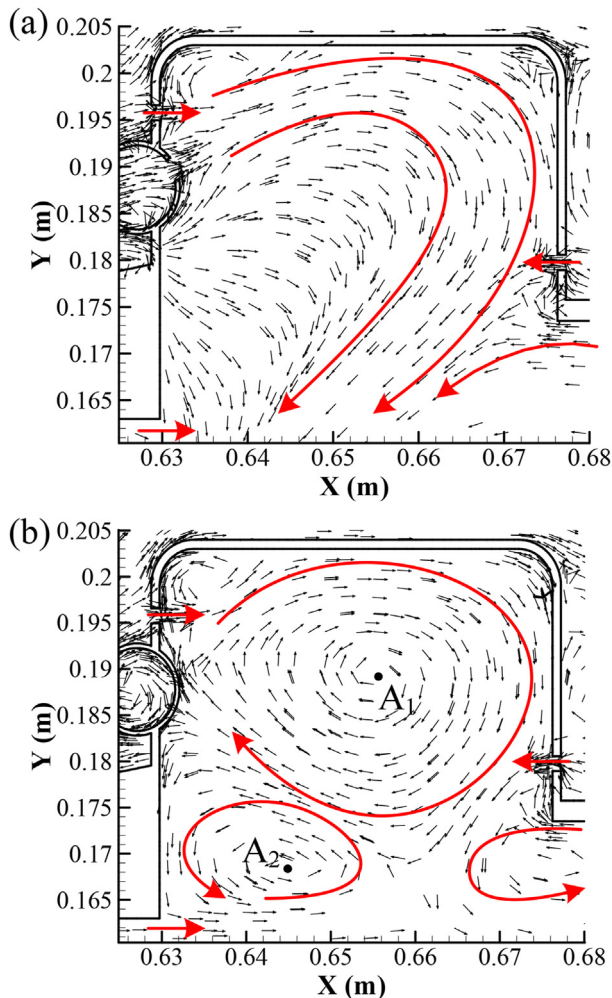


Fig. 12. The velocity vector graph of the cavity in the Case 1 at different sections of: (a) $z = 0$, (b) $z = 20$ mm.

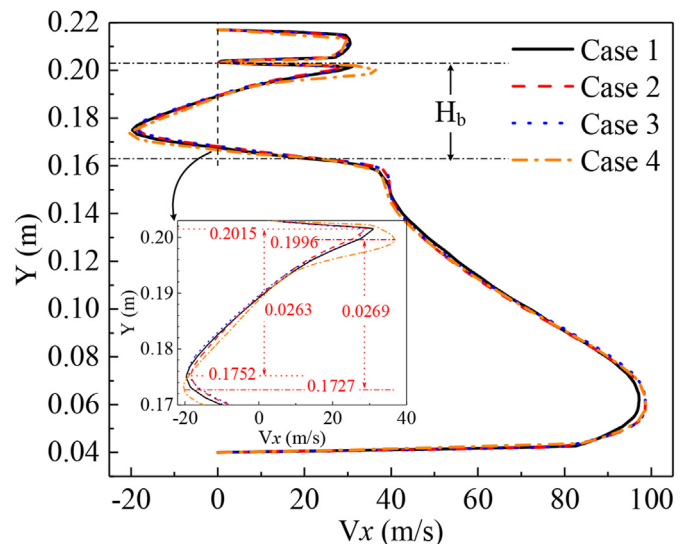


Fig. 14. Radial profiles of axial velocity at $x = 653$ mm in the plane of $z = 20$ mm.

$z = 20$ mm are painted to evaluate the size of the primary vortex in Fig. 14. The four velocity profiles fluctuate in the y -axis range of 0.163 m–0.203 m, marked as the fore-wall height, H_b , in the cavity. Besides, the distance between the point of the maximum and minimum V_x can commendably reflect the height of the primary vortex size. It is noteworthy that the axial velocity increases from 0 to ~35 m/s in the y -axis range of 0.203 m–0.20 m, while the V_x has a rapid drop for $y = 0.20$ –0.17 m, then the axial velocity changes from the negative to the positive and finally approaches the value of mainstream velocity with the y -coordinate moving from secondary vortex to the mainstream. In the $z = 20$ mm section, the sizes of the primary vortex in Case 1 to Case 4 are the same, in which the largest and shortest heights of the primary vortex are 26.9 mm and 26.3 mm, respectively. This strongly indicates that the time-scale theory based on the flow field structure cannot explain the variation in the lean ignition and lean blowout performance at the same inlet Mach number. Thus, the atomizer's characteristics must be excavated to understand the effect of the inlet structure parameter on flame stabilization.

3.3. Characteristic of atomizer and analysis

From an analysis of lean blowout data acquired from a large number of aircraft combustion chambers, the following equation for lean ignition and lean blowout fuel/air ratios, q_{IG} and q_{LBO} , was derived by Lefebvre [42].

$$q_{IG} = \left[\frac{E}{C_c} \right] \times \left[\frac{\dot{m}_a}{p_3^{1.5} \exp(T_3/300)} \right] \times \left[\frac{D_0^2}{\lambda_r H} \right] \quad (5)$$

$$q_{LBO} = \left[\frac{R}{C_{pz}} \right] \times \left[\frac{\dot{m}_a}{p_3^{1.3} \exp(T_3/300)} \right] \times \left[\frac{D_0^2}{\lambda_r H} \right] \quad (6)$$

where E and R are the combustor reference parameter, C_c and C_{pz} are the volumes of the combustor, \dot{m}_a is the mass flow rate of air, P_3 and T_3 are the pressure and temperature of combustor respectively, D_0 is the mean drop size, also Sauter mean diameter (SMD), H_r is the lower calorific value, and λ_r is the effective evaporation.

Here, C_c and C_{pz} are constant, which are only related to the combustor structure. Besides, P_3 and H_r are 0.101 MPa and 43,145 kJ/kg, respectively. The fuel/air ratio thus becomes

$$q_{IG\&LBO} \propto \frac{\dot{m}_a SMD_{LBO}^2}{\lambda_r \exp(T_3/300)} \quad (7)$$

If the inlet temperature and Mach number of the combustor remain unchanged, then the temperature of the fuel/air mixture ignited remains intact, so λ_r is approximately constant. According to Eq. (7), The relationship between the equivalence ratio and SMD is

$$\phi_{IG\&LBO} \propto SMD^2 \quad (8)$$

Many factors affect SMD, including nozzle structure, physical properties of the fuel, pressure drop and aerodynamic force, etc. [42]. Multitudinous studies of plain orifice have proved that the SMD of primary spray is negatively correlated with the pressure drop, while the SMD of secondary spray can be characterized by Weber number, expressed as

$$SMD \propto \frac{1}{\Delta P_{fuel}^a} \quad (9)$$

$$We_{crit} = \frac{\rho_{air} \bar{u}_{air}^2}{\sigma_{fuel} / D_{max}} \quad (10)$$

where $\rho_{air} \bar{u}_{air}^2$ is the disruptive aerodynamic force, σ_{fuel} / D_{max} is the consolidating surface tension force.

According to Lefebvre, $We_{crit} = 1.04$. Hence

$$D_{max} = 1.04 \sigma_{fuel} / \rho_{air} \bar{u}_{air}^2 \quad (11)$$

The principle of fuel drop atomization in AMI is mainly the interaction between airflow and fuel pressure drop. Keeping the equivalence ratio unchanged, the growth of Mach number will lead to an increase in the fuel mass flow rate, and the fuel pressure drop, ΔP_{fuel} will enlarge, which has excellent effectiveness in SMD. Simultaneously, the enhanced aerodynamic force, $\rho_{air} \bar{u}_{air}^2$, contributed by the increase of Mach number, promotes the secondary atomization, reducing the SMD. Similarly, the rise in fuel pressure drop is directly provided by increasing the equivalence ratio, causing a diminution of the SMD.

The droplet-size distribution and volumetric cumulative distribution at different Mach numbers with various equivalence ratios at the Z2 plane are depicted in Fig. 15. As expected, the SMD corresponding to the maximum value of the probability density distribution and 100% of the volumetric cumulative distribution drops with the increase of Mach number. Besides, the distribution of SMD narrows as the Mach number increases, which indicates that the percentage of the small size of fuel droplets increased in the total droplets. Concretely, with the growth of Mach number from 0.3 to 0.6 at $\phi = 0.4$, the peak value of the SMD probability density distribution curve gradually moved from 133.21 μm to 38.55 μm , illustrating that the most SMD reduces 71.06%. Meanwhile, the point, corresponding to the volumetric cumulative of 100%, decreases from 323 μm (the capacity of LPSA) to 207.43 μm with the Mach number varies from 0.3 to 0.6, which indicates that the D_{max} descends at least 35.78% with the increase of Mach number. It is worth noting that the probability density distribution of SMD is not sensitive to the influence of equivalence ratio, meaning that the impact of fuel pressure drop on SMD at the same Mach number can be ignored in all cases. Therefore, the increased Mach number leads to a decrease in SMD, which is also one of the reasons for improving the performance of lean ignition.

Fig. 16 shows SMD characteristics in three planes with Mach number measured by the AMI at 343 K with $\phi = 0.4$. The distribution of SMD profiles maintains the same trend in all three planes, which decreases as the Mach number increases. It is evident that the SMD gradually rises as the measurement position moves from section Z1 to Z3, which indicates that the SMD will be enlarged when the measurement position is away from the central section. The biggest SMD is 79.90 μm , happening at $Ma_2 = 0.3$ and section Z3, which is 22.08% and 30.06% larger than that in section Z2 and Z1. The reason is that the tiny droplets moving inside the evaporation tube can form aggregation quickly to become the big droplets so that the SMD is the largest in section Z3. Besides, the SMD in sections Z1 and Z2 are almost the same at a Mach number, and the maximum difference is 6.993 μm at $Ma_2 = 0.4$. As the Mach number varies from 0.3 to 0.6, the SMD in section Z2 decreased from 65.45 μm to 21.14 μm , reducing by 67.70%, reflecting that Mach number is opposed to the lean ignition and lean blowout equivalence ratio.

The relationship between Mach number and SMD with four equivalence ratios in section Z2 is plotted in Fig. 17. Similarly, the SMD follows similar curves of monotonically decreasing with the Mach number. Moreover, the SMD reduced from 81.11 μm to

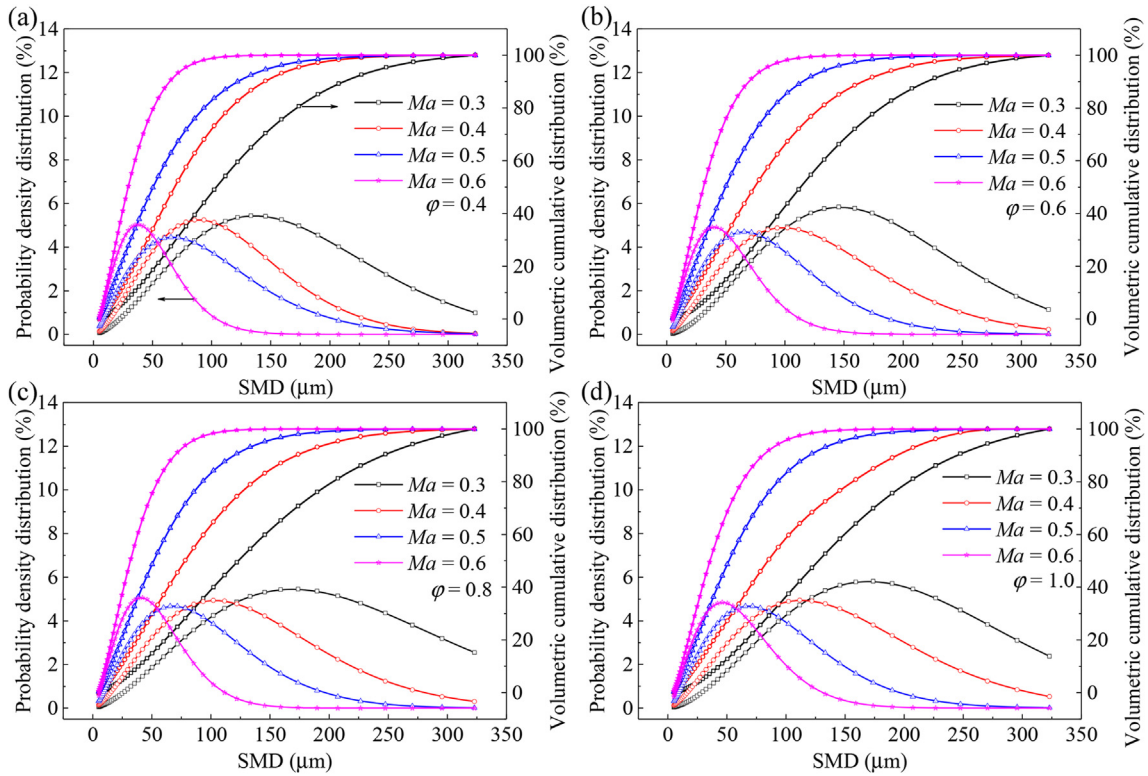


Fig. 15. Drop-size distribution and volumetric cumulative distribution at different Mach number with various equivalence ratios: (a) $\phi = 0.4$, (b) $\phi = 0.6$, (c) $\phi = 0.8$, (d) $\phi = 1.0$.

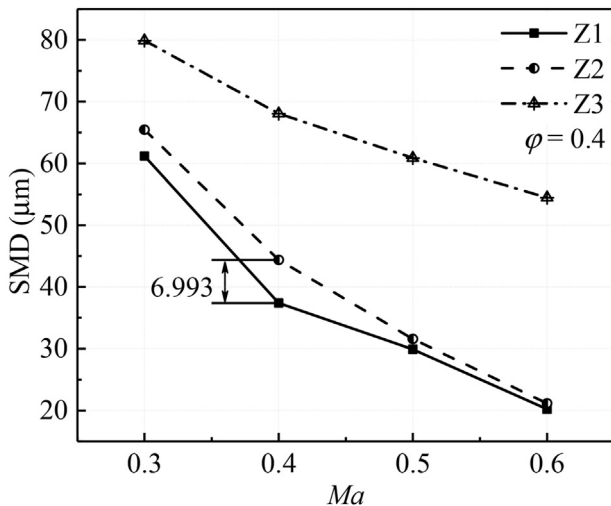


Fig. 16. The influence of inlet Mach number on SMD at different planes at $\phi = 0.4$.

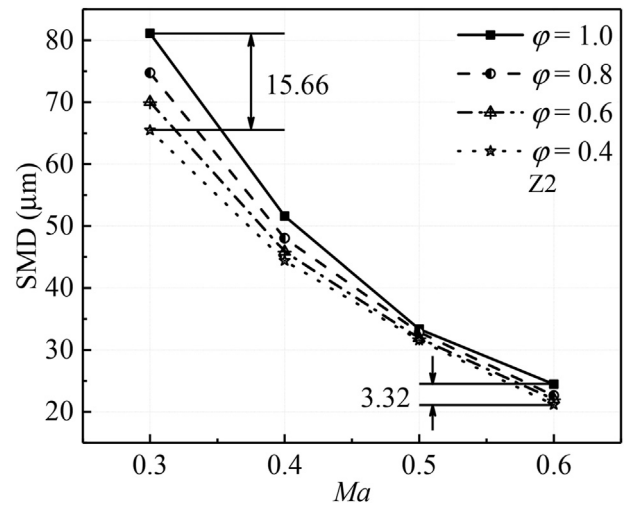


Fig. 17. The influence of inlet Mach number on SMD at plane Z2.

20.14 μm with the increase of Mach number from 0.3 to 0.6 overall. It is worth noting that the SMD in $\phi = 0.4$ is 15.66 μm (23.93%) smaller than that in $\phi = 1.0$ at $Ma_2 = 0.3$, while that value becomes to 3.32 μm (15.71%) at $Ma_2 = 0.6$. This phenomenon reflects that the effect of fuel pressure drop on the atomization quality is weaker than that of aerodynamic force. In other words, the SMD is greatly affected by the Mach number at the AMI inlet.

According to Eq. (8), there is a positive correlation between the ϕ and SMD^2 . Hence, when the inlet temperature is lower than the fuel evaporation temperature, such as $T_2 = 343 \text{ K}$ and $T_2 = 473 \text{ K}$, in which the SMD is mainly affected by aerodynamic force, $\rho_{air} \bar{u}_{air}^2$, the lean ignition equivalence ratio drops with the increase of Mach

number, as shown in Fig. 10(a) and (b). However, Eq. (7) shows that when the inlet temperature is higher than the fuel evaporation temperature of 573 K, the effective evaporation, λ_r , increases rapidly, and the aerodynamic force, $\rho_{air} \bar{u}_{air}^2$, has less influence on SMD. Simultaneously, an increase in Mach number will lead to a rapid shortening of fuel/air mixture residence time in the primary vortex, which is not conducive to flame stability. Therefore, a tendency of increasing first and then decrease has occurred in Fig. 10(c). Inversely, the exceptionally high temperature at the aglow wall of the evaporation tube is provided by the ignited flame, resulting in the highly effective evaporation, λ_r . Then, an excellent performance of evaporation and the small SMD is produced so that

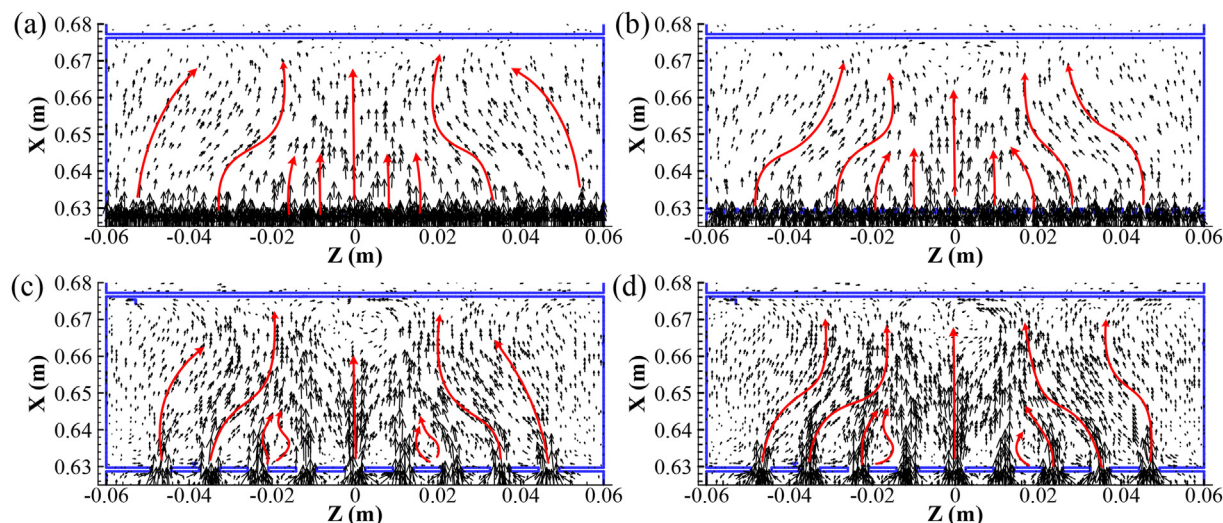


Fig. 18. The velocity vector graph in-plane Y1 with four inlet structures of the cavity in the fore-wall. (a) Case 1, (b) Case 2, (c) Case 3, (d) Case 4.

the influence of SMD on LBO can be eliminated. Therefore, the increased LBO equivalence ratio can be achieved by a shortened fuel/air mixture residence time, resulting in the growth of inlet Mach number.

As discussed above, the investigation of Jin [41] shows that the dual-vortex structure in the cavity with the strut is a three-dimensional feature. Fig. 18 shows the velocity vector graph in-plane Y1 with four inlet structures. The length of the arrow represents the magnitude of the local fluid velocity. The straight blue line is the boundary of the cavity structure, and the red arrow indicates the flow trend of the local fluid. As expected, the fluid's spiral movement in the cavity, flowing from both sides to the center, is attracted by the low-pressure area downstream of the ventral and radial V-gutter flameholder. The fluid on both sides of the cavity has a remarkable tendency to flow towards the center, which can be proved by the direction of the velocity vector. It can be seen that the unperturbed parallel-vectors appear near $x = 0.63$ m in Case 1, while the rotational velocity vectors happen in Case 3 and Case 4. The vector of Case 2 is slightly deflected, but no closed swirling vortex is formed. Besides, the scope of the reflux velocity vector gradually enlarges with the variation from Case 3 to Case 4, which indicates that the increase of distance between holes is conducive to the formation of recirculation zones downstream of plates. Furthermore, the perturbation of recirculation zones downstream of plates between holes can improve the quality of atomization and fuel/air mixing under the same condition, which can effectively optimize the performance of flame stabilization. Consequently, the velocity vectors near $x = 0.63$ m in Case 2 hold the same distribution as that in Case 3, leading to a virtually identical value of the lean ignition and lean blowout equivalence ratio, as shown in Figs. 10 and 11. Additionally, the lean ignition and lean blowout equivalence ratios in Case 4 are smaller than those in Case 1 to Case 3, which is contributed by the prominent recirculation zones. Then the increase of the size of the recirculation zone coincides with the increased ability of flame stabilization, which is very convictive evidence that the discrete holes in the fore-wall inlet structure of the cavity are beneficial to the improvement of the performance of the lean ignition and lean blowout.

4. Conclusions

Experiments and numerical calculations are conducted with

four types of primary air-jet in the cavity. The lean ignition and blowout limits are discussed with an accepted analysis attributed to the numerical fluid-structure. The droplet characteristics of air-assisted multi-point injector are measured for assistant analysis.

Compared with the benchmark scheme (slotted inlet), the largest Mach number, at which the flame can be stabilized, will be extended from 0.3 to 0.5 at the inlet temperature of 343 K if the discrete-hole inlet can be employed. Meanwhile, the lowest equivalence ratios of ignition and blowout are achieved by utilizing the discrete-hole inlet with the diameter and interval of 5.0 mm and 11.7 mm, respectively. These results indicated that the flame stability could be improved significantly by changing the primary air-jet form from slotted inlet to discrete-hole inlet. The lower equivalence ratios of ignition and lean blowout were obtained by a larger aperture under the same inlet passing area condition.

The decreasing trend of the lean ignition and blowout equivalence ratios, produced by the decreased inlet Mach number and temperature growth, is analyzed with the numerical fluid-structure and droplet-size distribution. This is evidence that the novel method optimizes the combustion performance by promoting the mixture of fuel and air, which has great reference value to combustor design.

The improvement of flame stability in the cavity by replacing the primary inlet structure from slotted to discrete-hole is technically feasible based on the experimental data. Future work aims to verify the effectiveness of the discrete-hole air-jet inlet under more realistic operating conditions, such as wider Mach number and lower pressure.

Author statements

Yakun Huang: Conceptualization, Methodology, Investigation, Software, Visualization, Data curation, Validation, Writing – original draft. **Xiaomin He:** Conceptualization, Writing- Reviewing and Editing, Supervision. **Huangwei Zhang:** Investigation, Visualization, Editing, Supervision. **Zhixin Zhu:** Investigation, Data curation. **Huangyu Zhu:** Investigation, Data curation.

Declaration of competing interest

The authors declare that they have no known competing financial interests or personal relationships that could have

appeared to influence the work reported in this paper.

Acknowledgments

This work was supported by the National Science and Technology Major Project, China (No. 2017-III-0008-0034). YH gratefully acknowledges the financial support from the China Scholarship Council, China (No. 201906830096).

References

- Huang W, Yan L, Tan JG. Survey on the mode transition technique in combined cycle propulsion systems. *Aero Sci Technol* 2014;39:685–91. <https://doi.org/10.1016/j.ast.2014.07.006>.
- Chen S, Chue RSM, Yu SCM, Schlüter JU. Spinning effects on a trapped vortex combustor. *J Propul Power* 2016;32:1133–45. <https://doi.org/10.2514/1.836005>.
- Bents DJ, Mockler T, Maldonado J, Harp JL, King JF, Schmitz PC. Propulsion system for very high altitude subsonic unmanned aircraft. *SAE Tech Pap* 1998. <https://doi.org/10.4271/981261>.
- Zhao D, Gutmark E, de Goey P. A review of cavity-based trapped vortex, ultra-compact, high-g, inter-turbine combustors. *Prog Energy Combust Sci* 2018;66:42–82. <https://doi.org/10.1016/j.pecs.2017.12.001>.
- Meyer TR, Brown MS, Fonov S, Goss LP, Gord JR, Shouse DT, et al. Optical diagnostics and numerical characterization of a trapped-vortex combustor. 38th AIAA/ASME/SAE/ASEE Jt Propuls Conf Exhib 2002. <https://doi.org/10.2514/6.2002-3863>.
- Jin Y, He X, Jiang B, Wu Z, Ding G, Zhu Z. Effect of cavity-injector/radial-strut relative position on performance of a trapped vortex combustor. *Aero Sci Technol* 2014;32:10–8. <https://doi.org/10.1016/j.ast.2013.12.014>.
- Shanbhogue SJ, Husain S, Lieuwen T. Lean blowoff of bluff body stabilized flames: scaling and dynamics. *Prog Energy Combust Sci* 2009;35:98–120. <https://doi.org/10.1016/j.pecs.2008.07.003>.
- Miao J, Fan Y, Wu W, Zhao S. Effect of air-assistant on ignition and flame-holding characteristics in a cavity-strut based combustor. *Appl Energy* 2021;283:116307. <https://doi.org/10.1016/j.apenergy.2020.116307>.
- Rongchun Z, Weijun F. Flow field measurements in the cavity of a trapped vortex combustor using PIV. *J Therm Sci* 2012;21:359–67. <https://doi.org/10.1007/s11630-012-0556-z>.
- Zhu Z, Huang Y, Zhang H, He X. Combustion performance in a cavity-based combustor under subatmospheric pressure. *Fuel* 2021;302:121115. <https://doi.org/10.1016/j.fuel.2021.121115>.
- Jiang P, He X. Experimental investigation of flow field characteristics in a mixed-flow trapped vortex combustor. *Aero Sci Technol* 2020;96:105533. <https://doi.org/10.1016/j.ast.2019.105533>.
- Liu C, Wang Z, Sun M, Wang H, Li P. Characteristics of a cavity-stabilized hydrogen jet flame in a model scramjet combustor. *AIAA J* 2019;57:1624–35. <https://doi.org/10.2514/1.J057346>.
- Merlin C, Domingo P, Vervisch L. Immersed boundaries in large eddy simulation of compressible flows. *Flow. Turbul Combust* 2013;90:29–68. <https://doi.org/10.1007/s10494-012-9421-0>.
- Jiang P, He X. Ignition characteristics of a novel mixed-flow trapped vortex combustor for turboshaft engine. *Fuel* 2020;261:116430. <https://doi.org/10.1016/j.fuel.2019.116430>.
- Choubey G, Devarajan Y, Huang W, Mehar K, Tiwari M, Pandey KM. Recent advances in cavity-based scramjet engine- a brief review. *Int J Hydrogen Energy* 2019;44:13895–909. <https://doi.org/10.1016/j.ijhydene.2019.04.003>.
- Roquemore WM, Shouse D, Burrus D, Johnson A, Cooper C, Duncan B, et al. Trapped vortex combustor concept for gas turbine engines. 39th AIAA/ASME/SAE/ASEE Jt Propuls Conf Exhib 2001.
- Zhang RC, Fan WJ, Xing F, Song SW, Shi Q, Tian GH, et al. Experimental study of slight temperature rise combustion in trapped vortex combustors for gas turbines. *Energy* 2015;93:1535–47. <https://doi.org/10.1016/j.energy.2015.09.122>.
- Li M, He X, Zhao Y, Jin Y, Yao K, Ge Z. Performance enhancement of a trapped-vortex combustor for gas turbine engines using a novel hybrid-atomizer. *Appl Energy* 2018;216:286–95. <https://doi.org/10.1016/j.apenergy.2018.02.111>.
- Ezhil Kumar PK, Mishra DP. Numerical investigation of the flow and flame structure in an axisymmetric trapped vortex combustor. *Fuel* 2012;102:78–84. <https://doi.org/10.1016/j.fuel.2012.06.056>.
- Zhao Y, He X, Li M. Effect of mainstream forced entrainment on the combustion performance of a gas turbine combustor. *Appl Energy* 2020;279:115824. <https://doi.org/10.1016/j.apenergy.2020.115824>.
- Zhang RC, Bai NJ, Fan WJ, Huang XY, Fan XQ. Influence of flame stabilization and fuel injection modes on the flow and combustion characteristics of gas turbine combustor with cavity. *Energy* 2019;189. <https://doi.org/10.1016/j.energy.2019.116216>.
- Xing F, Kumar A, Huang Y, Chan S, Ruan C, Gu S, et al. Flameless combustion with liquid fuel: a review focusing on fundamentals and gas turbine application. *Appl Energy* 2017;193:28–51. <https://doi.org/10.1016/j.apenergy.2017.02.010>.
- Straub DL, Casleton KH, Lewis RE, Sidwell TG, Maloney DJ, Richards GA. Assessment of rich-burn, quick-mix, lean-burn trapped vortex combustor for stationary gas turbines. *J Eng Gas Turbines Power* 2005;127:36–41. <https://doi.org/10.1115/1.1789152>.
- Hsu K, Goss LP, Trump DD, Roquemore WM. AIAA 95-0810 performance of a trapped-vortex combustor 33rd aerospace sciences meeting and exhibit. 1995.
- Zhu YX, He XM, Ye ZY, Jiang P. Experimental researches on lean blowoff performance of a variable geometry single-cavity trapped vortex combustor. *Tuijin Jishu/Journal Propuls Technol* 2018;39:1347–53. <https://doi.org/10.13675/j.cnki.tjjs.2018.06.018>.
- Vilkinis P, Pedišius N. Analysis of reattachment length dynamics in cavities. *Exp Therm Fluid Sci* 2020;119. <https://doi.org/10.1016/j.exptthermfluidsci.2020.110211>.
- Huang Y, He X, Zhu Z, Zhu H. Inlet pressure effects on subatmospheric flame stabilization with an optimum size of a cavity-based combustor. *Int J Aerosp Eng* 2020;2020. <https://doi.org/10.1155/2020/4126753>.
- Zhao Y, He X, Xiao J, Li M. Effect of cavity-air injection mode on the performance of a trapped vortex combustor. *Aero Sci Technol* 2020;106:106183. <https://doi.org/10.1016/j.ast.2020.106183>.
- Li M, He X, Zhao Y, Jin Y, Ge Z, Huang W. Effect of strut length on combustion performance of a trapped vortex combustor. *Aero Sci Technol* 2018;76:204–16. <https://doi.org/10.1016/j.ast.2018.02.019>.
- Huang Y, He X, Jiang P, Zhu H. Effect of non-uniform inlet velocity profile on flow field characteristics of a bluff body. *Exp Therm Fluid Sci* 2020;118. <https://doi.org/10.1016/j.exptthermfluidsci.2020.110152>.
- Zhu Z, He X, Xue C, Hong L, Zhu Y, Song Y. Experimental investigations on combustion characteristics of a cavity piloted augmentor of the turbine-based combined cycle engine. *Proc Inst Mech Eng Part G J Aerosp Eng* 2015;229:2024–34. <https://doi.org/10.1177/0954410014564202>.
- Zhang Y, He X, Zhu H. Study on atomization performance of multi-orifice air-assisted plain jet atomizers. *Fuel* 2021;286:119428. <https://doi.org/10.1016/j.fuel.2020.119428>.
- Jin Y, Li Y, He X, Zhang J, Jiang B, Wu Z, et al. Experimental investigations on flow field and combustion characteristics of a model trapped vortex combustor. *Appl Energy* 2014;134:257–69. <https://doi.org/10.1016/j.apenergy.2014.08.029>.
- Wu Z, Jin Y, He X, Xue C, Hong L. Experimental and numerical studies on a trapped vortex combustor with different struts width. *Appl Therm Eng* 2015;91:91–104. <https://doi.org/10.1016/j.applthermaleng.2015.06.068>.
- Yang S, Zhang C, Lin Y, Xue X, Gan X. Experimental investigation of the ignition process in a separated dual-swirl spray flame. *Combust Flame* 2020;219:161–77. <https://doi.org/10.1016/j.combustflame.2020.05.010>.
- Shouse DT. Trapped vortex combustion technology. 2013. 12-05] Http Ff Soliton, Ae Gatech, Edu/People/Lsankar/MITE Work Pdf 2000.
- Katta VR, Roquemore WM. Study on trapped-vortex combustor - effect of injection on flow dynamics. *J Propul Power* 1998;14:273–81. <https://doi.org/10.2514/2.5286>.
- Zhang RC, Huang XY, Fan WJ, Bai NJ. Influence of injection mode on the combustion characteristics of slight temperature rise combustion in gas turbine combustor with cavity. *Energy* 2019;179:603–17. <https://doi.org/10.1016/j.energy.2019.04.223>.
- Li M, He X, Zhao Y, Jin Y, Ge Z, Sun Y. Dome structure effects on combustion performance of a trapped vortex combustor. *Appl Energy* 2017;208:72–82. <https://doi.org/10.1016/j.apenergy.2017.10.029>.
- Jin Y, He X, Zhang J, Jiang B, Wu Z. Numerical investigation on flow structures of a laboratory-scale trapped vortex combustor. *Appl Therm Eng* 2014;66:318–27. <https://doi.org/10.1016/j.applthermaleng.2014.02.030>.
- Lefebvre AH, Ballal DR. Gas turbine combustion. third ed. New York: Taylor & Francis Group; 2010.